

Received 3 June 2022, accepted 28 June 2022, date of publication 30 June 2022, date of current version 6 July 2022.

Digital Object Identifier 10.1109/ACCESS.2022.3187553

RESEARCH ARTICLE

# Very-Wide-Band Six-Port Single-Patch Antenna With Six Uncorrelated Waves for MIMO Access Points

KIN-LU WONG<sup>1</sup>, (Fellow, IEEE), ZONG-WEN TSO<sup>1</sup>, (Student Member, IEEE), AND WEI-YU LI<sup>2</sup>, (Member, IEEE)

<sup>1</sup>Department of Electrical Engineering, National Sun Yat-sen University, Kaohsiung 80424, Taiwan

<sup>2</sup>Information and Communications Research Laboratories, Industrial Technology Research Institute, Hsinchu 31057, Taiwan

Corresponding author: Kin-Lu Wong (wongkl@mail.nsysu.edu.tw)

This work was supported by the Ministry of Science and Technology, Taiwan, under Grant MOST 111-2218-E-110-003.


**ABSTRACT** A very-wide-band six-port circular patch antenna for MIMO access-point application is presented. The six-port patch antenna can radiate six uncorrelated waves (envelope correlation coefficients  $<0.01$ ) in a very wide band of about 3.1-7.2 GHz (fractional bandwidth about 80%), which can be applied to cover 3.3-5.0 GHz for 5G communication and 6.425-7.125 GHz for possible new mobile band. The six uncorrelated waves are generated by using six coupling L-strip feeds to respectively excite six  $60^\circ$ -resonant sectors isolated by six radial shorting metal walls connecting the circular patch to the ground plane. Enhanced port isolation ( $>20$  dB) is obtained by embedding six decoupling radial slots along the centerlines of the six  $60^\circ$ -resonant sectors, with very small effects on the excited resonant modes. Details of the proposed six-port six-uncorrelated-wave single-patch MIMO antenna are addressed. Experimental results of the fabricated prototype are presented.

**INDEX TERMS** MIMO access-point antennas, six-port single-patch MIMO antennas, wideband multi-port single-patch antennas, wideband patch antennas.

## I. INTRODUCTION

The wideband multi-port single-patch antenna (SPA) has the attractive feature of generating multiple uncorrelated waves in a compact antenna structure for wideband multi-input-multi-output (MIMO) applications [1]–[10]. The three-port SPAs reported in [1]–[4] can radiate three uncorrelated waves by exciting the circular patch [1] or Y-shaped patch [2], [3] or equilateral triangular patch [4] in three different polarization planes with the port isolation larger than about 15 dB over an operating band of about 3.3-4.2 GHz (fractional bandwidth about 24%).

The four-port SPAs radiating four uncorrelated waves have also been reported [5]–[9]. The shorting metal walls (or in the form of multiple shorting pins [6]) are used to achieve four resonant quadrants in a square patch [5], [6] to achieve good port isolation to generate four uncorrelated waves. The

The associate editor coordinating the review of this manuscript and approving it for publication was Chinmoy Saha .

port isolation of the four ports larger than 15 dB over a wide band of 3.3-5.0 GHz (fractional bandwidth about 42%) for fifth-generation (5G) MIMO operation is obtained [5]. In [7], the four-port SPA with an annular-ring (AR) patch generating four uncorrelated waves in 3.3-5.0 GHz is reported. The AR patch is modified to have four isolated  $90^\circ$  resonant AR sectors to support the monopolar patch mode (MPA) [11] excitation for each port. Four uncorrelated waves with the port isolation larger than 15 dB over the wide band of 3.3-5.0 GHz are also achieved.

With the aid of an external feed network to excite multiple modes with enhanced port isolation, it has also been shown that the four-port SPA with a modified square patch or the four-port multi-mode antenna can generate four uncorrelated waves with port isolation larger than 20 dB over a wide band of 6.0-8.5 GHz (fractional bandwidth about 35%) [8]. A similar four-port multi-mode antenna covering a wide band of 3.0-6.0 GHz (fractional bandwidth about 67%) with high port isolation ( $>20$  dB) has also been reported [9].

**TABLE 1. Comparison of reported wideband six-port single-patch antennas with six uncorrelated waves for MIMO access points.**

Ref.	[10]	This work (Design B)
Operating bandwidth	6.0-8.5GHz (35%)	3.1-7.2 GHz (80%)
Antenna height	12.5 mm ( $0.25\lambda$ @6.0GHz)	14 mm ( $0.15\lambda$ @3.3GHz)
Patch shape/size	Square patch, side length 45 mm ( $0.90\lambda$ @6.0GHz)	Circular patch, diameter 68 mm ( $0.75\lambda$ @3.3GHz)
Resonant patch area including the feed for each port (total area/6)	$0.135\lambda^2$ @6.0GHz (side length 45 mm)	$0.11\lambda^2$ @3.3GHz (diameter 83 mm)
Antenna efficiency	44-64% for Ports 1-6 at 7.25 GHz	> 85% for Ports 1-6 in the operating band
ECC	< 0.05	< 0.01
Port isolation	> 20 dB	> 20 dB
External feed network	Required, multi-layer technology applied	No
All-metal structure	No	Yes

For the multi-port SPA to have more than four isolated ports to generate more uncorrelated waves over a wide band is even more challenging. Recently, based on the multi-mode MIMO antenna design concept [8], [9], a six-port SPA or a six-port multi-mode antenna has been reported [10]. The six ports collocated in a modified square patch can generate six uncorrelated waves in a wide band of 6.0-8.5 GHz with the port isolation larger than 20 dB. However, the antenna efficiency of the six radiating waves is only about 44%-64% [10], which will limit its practical application. This characteristic is largely in part owing to the required large-size external feed network to excite multiple modes with enhanced port isolation. The large-size external feed network also complicates the antenna design.

In this study, a very-wide-band six-port SPA with a simple all-metal structure to generate six uncorrelated waves in about 3.1-7.2 GHz (fractional bandwidth about 80%) is presented. In addition to the simple all-metal structure, no external feed network as required in [10] is needed. The operating band has a fractional bandwidth larger than those reported in [1]-[10] for the multi-port SPAs and can be applied to cover 3.3-5.0 GHz for 5G MIMO operation [12], [13] and 6.425-7.125 GHz for possible new mobile band [14].

The proposed 6-port SPA is based on using a wideband circular patch antenna in which six radial shorting metal walls connects the circular patch to the ground plane to form six isolated 60°-resonant sectors. Six coupling L-strip feeds (Ports 1-6) are then applied to respectively excite the six isolated resonant sectors to generate six uncorrelated waves over the wide operating band. The antenna height and the resonant patch area including the feed for each port are all smaller than those in the reported six-port multi-mode antenna [10] as shown in Table 1.

Additionally, the obtained envelope correlation coefficients (ECCs) of the six generated waves in the proposed

antenna is less than 0.01. High port isolation of the six ports to be larger than 20 dB is also obtained over the wide band by embedding six radial decoupling slots along the centerlines of the six 60°-resonant sectors. The obtained antenna efficiency of the six-port SPA is also larger than 85% over the antenna's wide operating band. A comparison of the proposed six-port SPA and the reported related antenna are also listed in Table 1.

Details of the six-port SPA with six uncorrelated waves are addressed in the study. The six-port SPA is also fabricated and studied. The experimental results are presented and discussed. The proposed six-port SPA has the advantages of simple all-metal structure, high port isolation (>20 dB), very low ECCs (<0.01), high antenna efficiency (>85%), and wide operating band (about 80% in fractional bandwidth) and is expected to be suitable for MIMO access-point applications.

## II. SIX-PORT SIX-UNCORRELATED-WAVE SINGLE-PATCH ANTENNA

Figs. 1 and 2 show the very-wide-band six-port circular SPA with six uncorrelated waves. Two designs of the six-port SPA (Design A in Fig. 1 and Design B in Fig. 2) with Ports 1-6 are presented. The dimensions of both designs are the same, except that there are six radial decoupling wide slots embedded in the circular patch to achieve enhanced port isolation in Design B.

As shown in the figure, the SPA has a simple structure consisting of a circular patch, six shorting metal walls, and six L-shape feed strips. The circular patch has a diameter of 68 mm (about  $0.75\lambda$  at 3.3 GHz, the desired lowest operating frequency in the study). The circular patch is mounted 13.8 mm above the ground plane of diameter 110 mm (about  $1.2\lambda$  at 3.3 GHz). Note that the proposed six-port SPA is an all-metal structure with the 0.2 mm thick copper plate used. The total antenna height above the ground plane is therefore 14 mm (about  $0.15\lambda$  at 3.3 GHz), including the copper-plate thickness.

The six shorting metal walls are of same dimensions (length 27 mm, width 13.8 mm) and connect the circular patch to the ground plane. Each metal wall is aligned in the radial direction and spaced by 60° to its two nearby metal walls. Six 60°-resonant sectors (Sectors 1-6) are therefore formed between the circular patch and the ground plane. Since each resonant sector is bounded by two metal walls spaced by 60°, it is expected to support the quarter-wavelength resonance in two different directions, which is similar to the  $TM_{1/2,1/2}$  mode excited in the 90°-resonant quadrant in the four-port SPA reported in [5]. For this reason, the corresponding resonant mode excited in each 60°-resonant sector in this study is denoted as the 60°- $TM_{1/2,1/2}$  mode.

The six L-shape feed strips also have same dimensions and are placed along the circumference of the circular patch to respectively excite Sectors 1-6. Each L-shape feed strip consists of a vertical rectangular strip (13 mm × 9 mm) and a horizontal rectangular strip (7 mm × 4 mm). The vertical

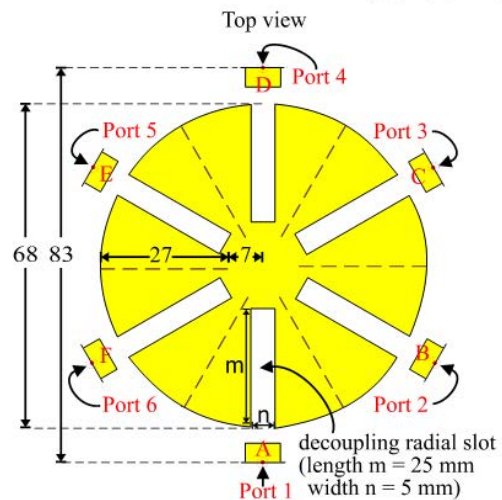
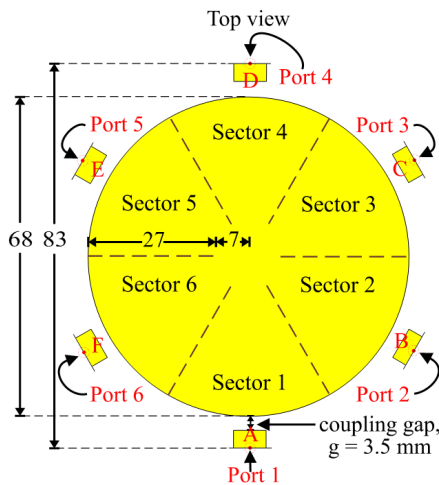
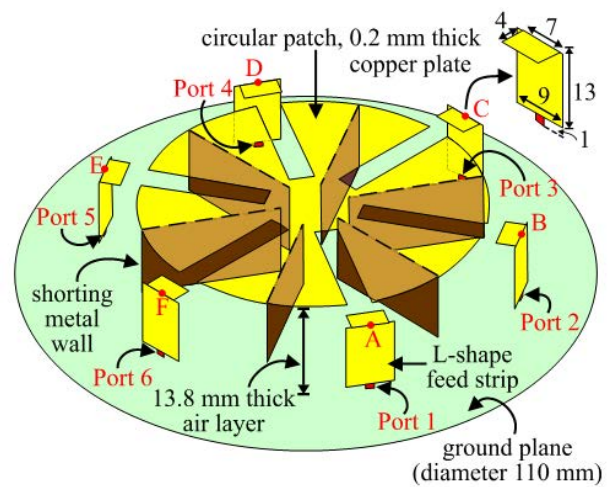
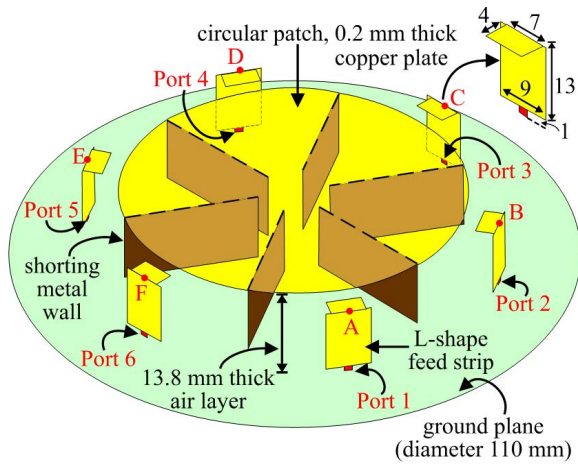


**FIGURE 1.** Geometry of the very-wide-band six-port circular SPA with six uncorrelated waves (Design A).

**FIGURE 2.** Geometry of the very-wide-band six-port circular SPA with six uncorrelated waves (Design B).

strip is at a position of 41.5 mm to the antenna center, while the horizontal strip is in the same plane as the circular patch.

Through a coupling gap ( $g$ ) of 3.5 mm, each L-shape strip positioned at the centerline of a  $60^\circ$ -resonant sector successfully excites the  $60^\circ$ - $\text{TM}_{1/2,1/2}$  mode. Effects of varying the coupling gap on the excited resonant mode will be analyzed later. Also, the wide width (9 mm) of the vertical strip can lead to a much decreased input inductance seen at the feed port, which helps to achieve a smooth variation of the input impedance over a wide band. This in turn helps to obtain a wide operating band for the proposed six-port SPA.

By including the L-shape feed strips and the circular patch, the total diameter of the 6-port SPA studied here is 83 mm (about  $0.91\lambda$  at 3.3 GHz). The average size for each port including the L-shape feed strip is therefore about  $0.11\lambda^2$ , which is smaller than that (about  $0.135\lambda^2$ ) in the 6-port multimode antenna [10] (also see the comparison listed in Table 1).

For Design B, in which along the centerline of each  $60^\circ$ -resonant sector, a radial wide slot of width 5 mm and length 25 mm (about  $0.275\lambda$  at 3.3 GHz) is embedded. The radial slot is placed along the centerline of each resonant

sector and will therefore be in parallel to the excited surface currents on the top patch for the  $60^\circ$ - $\text{TM}_{1/2,1/2}$  mode. In this case, it is expected that the radial slot will have small or negligible effects on the impedance matching or reflection coefficient of the excited resonant mode for each port. That is, Design B can have a similar wide operating band as Design A.

On the other hand, for each port excitation (for example, Port 1 for Sector 1), the radial slots in its two nearby resonant sectors (Sectors 2 and 6 with respect to Sector 1) will behave like a decoupling slot, when the slot length is adjusted to be around a quarter-wavelength of the desired frequency [15], [16] (around 3.3 GHz in this study). That is, for Port 1 excitation, the possible coupling of the excited surface currents on Sector 1 to Sectors 3-5 can be greatly suppressed, owing to the trapping effects of the decoupling slots in Sectors 2 and 6. The port isolation of Port 1 to Ports 3-5 can therefore be greatly enhanced. On the other hand, the isolation improvement of Port 1 to its two nearby ports (Ports 2 and 6) is relatively not so significant as Port 1 to Ports 3-5.

To verify the antenna performance and operating principle of the six-port SPA with Designs A and B, a simulation study

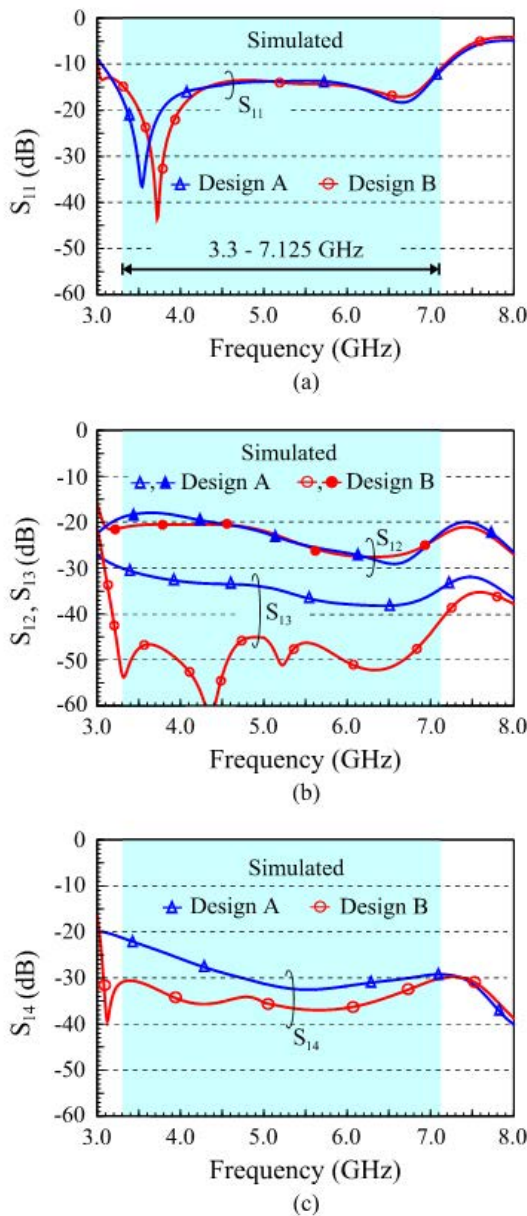


FIGURE 3. Simulated Parameters of Port 1 in Designs A and B. (a)  $S_{11}$ . (b)  $S_{12}(=S_{16})$ ,  $S_{13}(=S_{15})$ . (c)  $S_{14}$ .

using the commercially available tool of High Frequency Structure Simulator (HFSS) version 19.1 is conducted [17]. The simulated  $S$  parameters of Port 1 in Designs A and B are presented in Fig. 3. The colored region in the figure indicates the desired frequency range of 3.3-7.125 GHz for possible practical applications covering 3.3-5.0 GHz for 5G MIMO operation [12], [13] and 6.425-7.125 GHz for possible new mobile band [14]. Note that, owing to the symmetric structure of Ports 1-6 in the proposed design, only the results of Port 1 are shown.

As seen in the reflection coefficient  $S_{11}$  in Fig. 3(a), a very wide band of about 3.1-7.2 GHz (fractional bandwidth about 80%) with  $-10$  dB impedance matching is obtained for

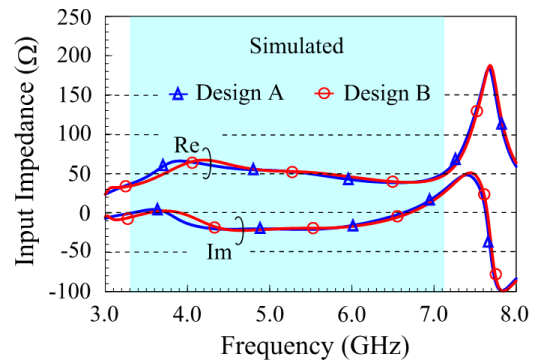


FIGURE 4. Simulated input impedance of Port 1 in Designs A and B.

Designs A and B. The very wide band is formed by two resonances at about 3.6 GHz and 6.6 GHz. The first resonance occurs slightly at a higher frequency for Design B than for Design A. This may be owing to the radial wide slots added in Design B, which slightly decreases the effective resonant length for the first resonance at a lower frequency. On the other hand, the second resonance at a higher frequency is almost the same for both designs. In general, the  $S_{11}$  for both designs are very similar and it can be concluded that the radial wide slots embedded in Design B show small effects on the impedance matching of the antenna.

The transmission coefficients  $S_{12}$  ( $= S_{16}$ ) and  $S_{13}$  ( $= S_{15}$ ) are presented in Fig. 3(b), while the transmission coefficients  $S_{14}$  is shown in Fig. 3(c). For Design A, the transmission coefficients are all less than about  $-18$  dB over the wide band. While for Design B, the  $S_{13}$  is significantly decreased from below  $-30$  dB to less than  $-40$  dB over the wide band. The  $S_{14}$  is also greatly decreased to be less than  $-30$  dB over the wide band for Design B. The  $S_{12}$  of Port 1 to its nearby port is also slightly decreased to be less than  $-20$  dB over the wide band for Design B. That is, all the port isolation for Design B is larger than 20 dB. The enhanced port isolation in Design B is mainly owing to the presence of the decoupling radial wide slots whose length is adjusted to be around a quarter-wavelength at around 3.3 GHz. The results of the simulated transmission coefficients verify the decoupling effects explained earlier in this section.

Fig. 4 shows the simulated input impedance seen at Port 1 in Designs A and B. In the desired wide band, smooth variations of the input resistance (Re) and input reactance (Im) are seen. The input resistance is slightly varied around 50 ohms, while the input reactance shows zero reactance at similar frequencies of the two resonances seen in Fig. 3(a). To analyze the two resonances seen in the antenna's impedance matching, Fig. 5 shows the simulated vector surface current distributions at 3.6 GHz and 6.6 GHz of Port 1 excitation in Design A, with other ports terminated to  $50 \Omega$ . The corresponding results for Design B are shown in Fig. 6.

Similar surface current distributions at the two frequencies for Designs A and B are observed. This confirms that the embedded radial wide slots for enhanced port isolation show

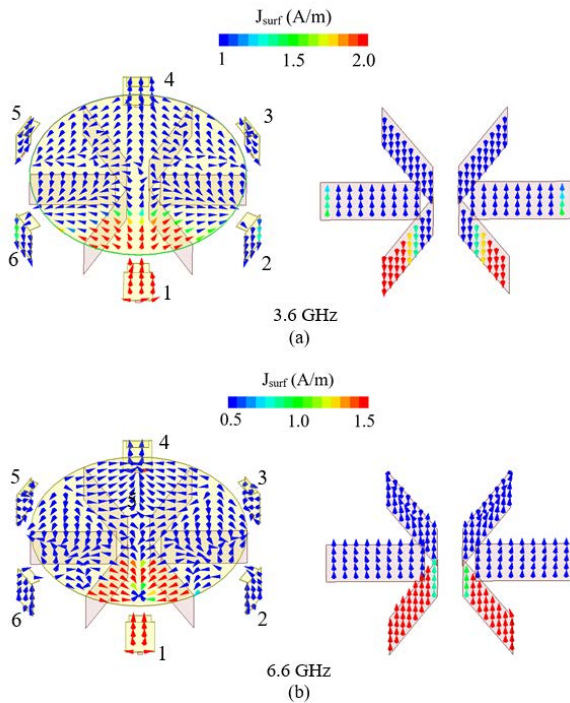


**FIGURE 5.** Simulated vector surface current distributions of Port 1 excitation in Design A. (a) 3.6 GHz and (b) 6.6 GHz.

small or negligible effects on the excited resonant modes of the antenna. Also, the surface currents are generally confined in Sector 1 for Port 1 excitation. This verifies the high port isolation seen in Fig. 3(b) and (c). The surface currents are also seen to be symmetric with respect to the centerline of Sector 1 and respectively toward both metal walls. This suggests that the resonant modes at 3.6 GHz and 6.6 GHz are both excited with quarter-wavelength resonance in two different directions, which is therefore denoted as the  $60^\circ$ - $\text{TM}_{1/2,1/2}$  mode here. In addition, since similar surface currents are excited at the two resonances at 3.6 GHz and 6.6 GHz, it is considered that the  $60^\circ$ - $\text{TM}_{1/2,1/2}$  mode with dual resonance [5] is generated in this study to form the wide operating band.

A parametric study for varying the dimensions of the decoupling radial wide slots to finely adjust the port isolation in the six-port SPA is also conducted. Fig. 7 shows the simulated  $S$  parameters of Port 1 as a function of the radial slot length in Design B. The results for the slot length ( $m$ ) varied from 21 mm to 25 mm are shown. The  $S_{11}$  shown in Fig. 7(a) shows very small variations, again indicating that the impedance matching is almost not affected by the radial wide slot in each resonant sector. As shown in Fig. 7(b), very small effects on the  $S_{12}$  ( $= S_{16}$ ) are seen.

Conversely, the dip in the  $S_{13}$  ( $= S_{15}$ ) near the lower-edge frequency of the operating band is shifted to a higher frequency with a decrease in the slot length. Similar behavior is seen for the  $S_{14}$  shown in Fig. 7(c). The results further confirm that, for Port 1 excitation in Sector 1, the radial wide slots in Sectors 2 and 6 behave like quarter-wavelength decoupling elements and they can be adjusted to suppress

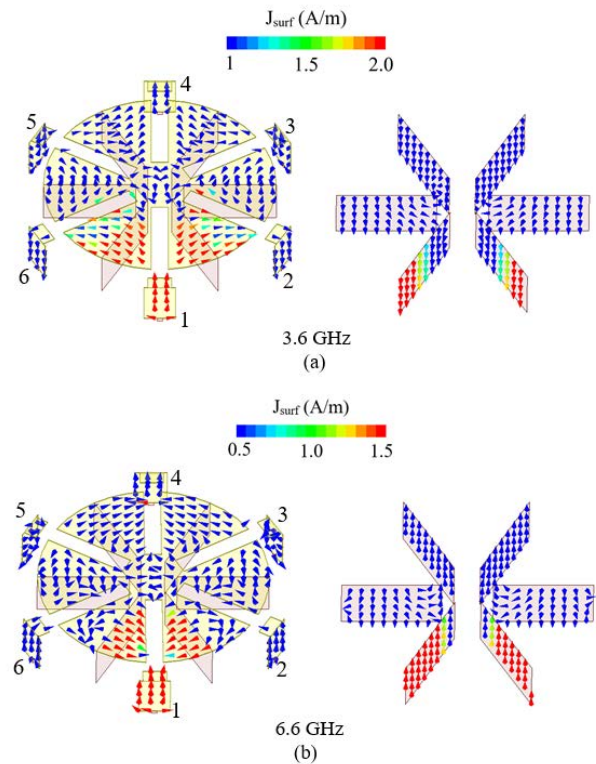


**FIGURE 6.** Simulated vector surface current distributions of Port 1 excitation in Design B. (a) 3.6 GHz. (b) 6.6 GHz.

the possible coupling of the excited surface currents from Sector 1 to Sectors 3, 4, and 5. Therefore, when the slot length is varied, the  $S_{13}$  ( $= S_{15}$ ) and  $S_{14}$  can be adjusted, with relatively small effects on the  $S_{12}$  ( $= S_{16}$ ).

Effects of varying the width of the radial wide slot are also studied. Fig. 8 shows the simulated  $S$  parameters of Port 1 as a function of the radial slot width in Design B. The results for the slot width ( $n$ ) varied from 1 mm to 5 mm are shown. Similar small effects on the  $S_{11}$  [see Fig. 8(a)] and the  $S_{12}$  ( $= S_{16}$ ) [see Fig. 8(b)] as observed in Fig. 6 are also seen. The effects on the  $S_{13}$  ( $= S_{15}$ ) in Fig. 8(b) and the  $S_{14}$  in Fig. 8(c) are also relatively large as in Fig. 6. From the simulation study, the dimensions of the decoupling wide slots are selected to be 25 mm  $\times$  5 mm in Design B to obtain high port isolation of Ports 1-6 to be larger than 20 dB over the wide operating band (about 3.1-7.2 GHz here). Note that although the  $S_{11}$  is about  $-10$  dB at about 3.0 GHz, the  $S_{12}$  is larger than  $-20$  dB around 3.0-3.1 GHz [see Fig. 8(a) and (b)]. Therefore, the operating band of Design B is considered to start from about 3.1 GHz here.

Effects of varying the coupling gap between the L-strip feed and the circular patch are also investigated. Fig. 9 shows the simulated  $S$  parameters of Port 1 for the coupling gap ( $g$ ) varied from 3.0 mm to 4.0 mm. In contrast to the results obtained in Figs. 6 and 7 for the decoupling radial wide slots, very small effects on the transmission coefficients are seen [see the  $S_{12}$  ( $= S_{16}$ ),  $S_{13}$  ( $= S_{15}$ ), and  $S_{14}$  in Fig. 9(b) and (c)].

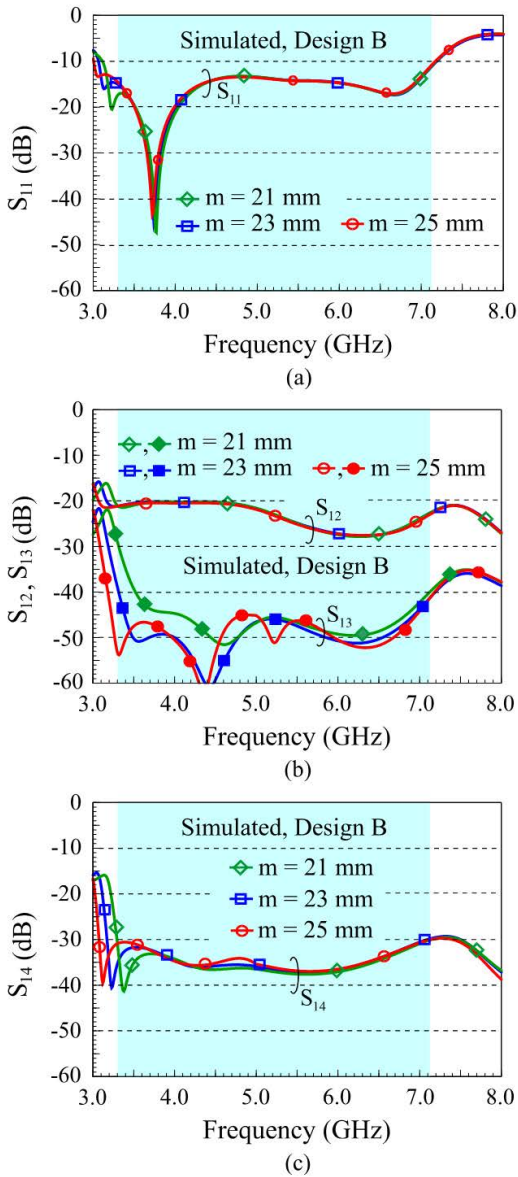


**FIGURE 7.** Simulated  $S$  parameters of Port 1 as a function of the radial slot length ( $m$ ) in Design B. (a)  $S_{11}$ . (b)  $S_{12}$  ( $= S_{16}$ ),  $S_{13}$  ( $= S_{15}$ ). (c)  $S_{14}$ .

On the other hand, it is seen that the  $S_{11}$  in Fig. 9(a) can be adjusted by varying the coupling gap. With a smaller coupling gap, it is expected that the capacitive input reactance seen at the feed port will be larger. This will in turn cause the first resonance to be shifted to lower frequencies. While for the second resonance at about 6.6 GHz, which has a smaller wavelength, the variation in the coupling gap will have smaller effects on varying the effective capacitive input reactance seen at the feed port. Smaller variations on the  $S_{11}$  for the second resonance at about 6.6 GHz is therefore observed. From the parametric study in Figs. 7-9, it indicates that the dimensions of the radial wide slots and the coupling gaps can be varied to respectively finely adjust the port isolation and impedance matching of Ports 1-6 in Design B.

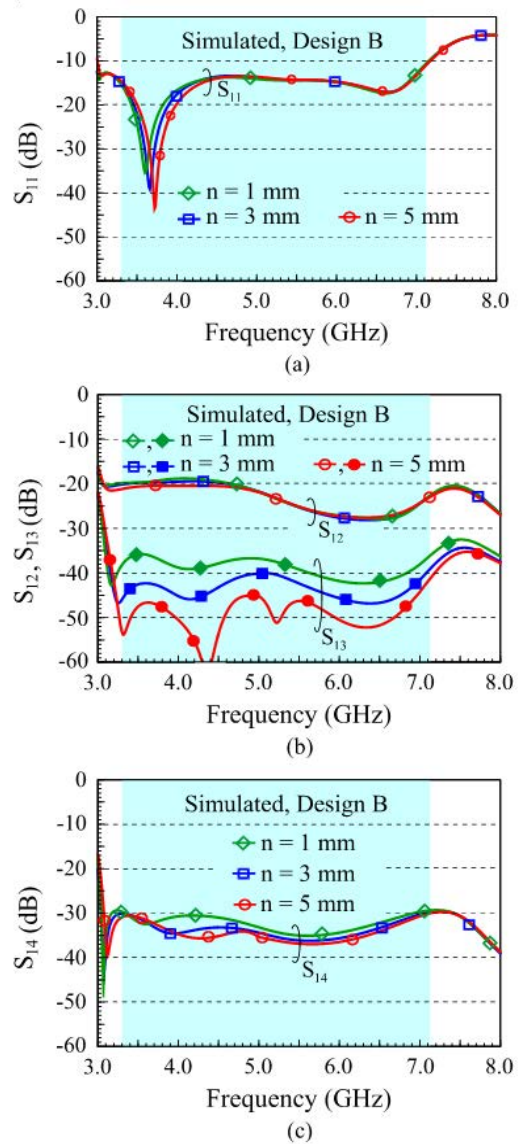


**FIGURE 8.** Simulated  $S$  parameters of Port 1 as a function of the radial slot width ( $n$ ) in Design B. (a)  $S_{11}$ . (b)  $S_{12}$  ( $= S_{16}$ ),  $S_{13}$  ( $= S_{15}$ ). (c)  $S_{14}$ .

For considering the six-port SPA as a whole to transmit six MIMO streams, the simulated total active reflection coefficient (TARC) [5], [18] for Design B is shown in Figs. 10 and 11. The results in Fig. 10 are for the assumption that the six MIMO streams are synchronized to have same amplitude and phase. The results show that the TARC is also less than  $-10$  dB over the desired wide operating band. Those shown in Fig. 11 are for the case that Ports 1-6 have an interval of 30 degrees in phase. Again, the TARC is also almost less than  $-10$  dB over the wide band. This characteristic is expected to be owing to the high port isolation of Ports 1-6 in Design B.

In Fig. 12, the simulated mean effective gain (MEG) [19] of Port 1 in Design B is presented. The results are obtained by assuming the isotropic uniform incident wave condition. Also, owing to the symmetric structure of Ports 1-6, the

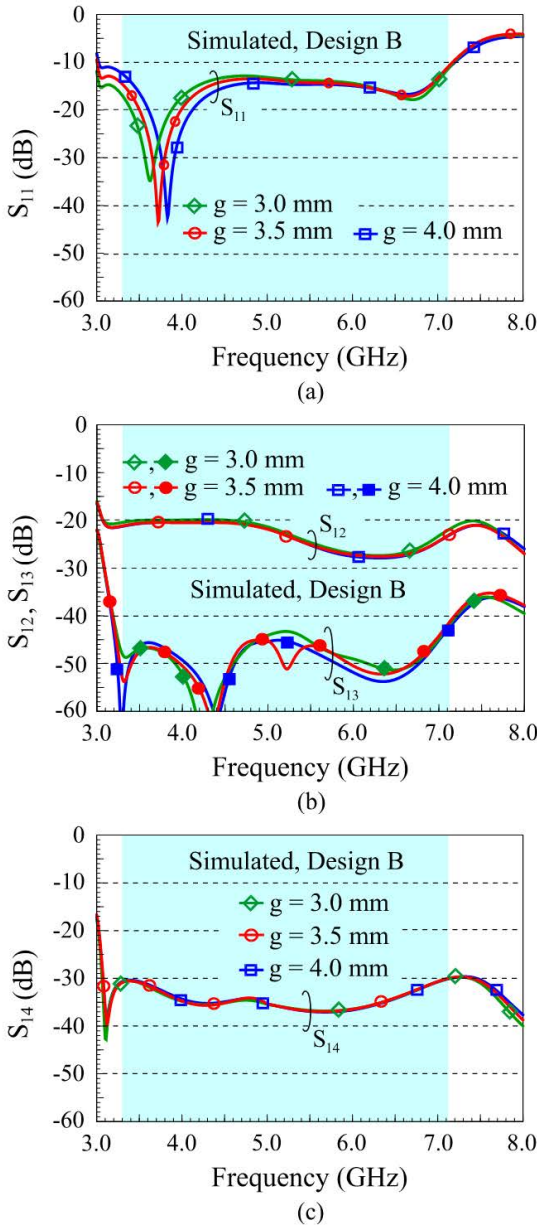


**FIGURE 9.** Simulated  $S$  parameters of Port 1 as a function of the coupling gap ( $g$ ) between the L-strip feed and the circular patch. (a)  $S_{11}$ . (b)  $S_{12}$  ( $= S_{16}$ ),  $S_{13}$  ( $= S_{15}$ ). (c)  $S_{14}$ .

simulated MEG values of Ports 2-6 are same as that of Port 1. The MEG values over the wide band are very slightly varied.

Fig. 13 shows the channel capacity loss (CLL) [20], [21] between Ports  $i$  and  $j$  in Design B. Typical results of  $CLL_{12}$  (between Ports 1 and 2),  $CLL_{13}$  (between Ports 1 and 3), and  $CLL_{14}$  (between Ports 1 and 4) are demonstrated. Note that, owing to the symmetric structure of Design B, the  $CLL_{12}$  and  $CLL_{13}$  are respectively same as the  $CLL_{16}$  and  $CLL_{15}$ . The CLL values in the wide band of 3.3-7.125 GHz are less than about 0.2 bits/s/Hz, which are less than 0.4 bits/s/Hz for practical application requirement and are expected to ensure high throughput of the proposed MIMO antenna in practical applications [21].

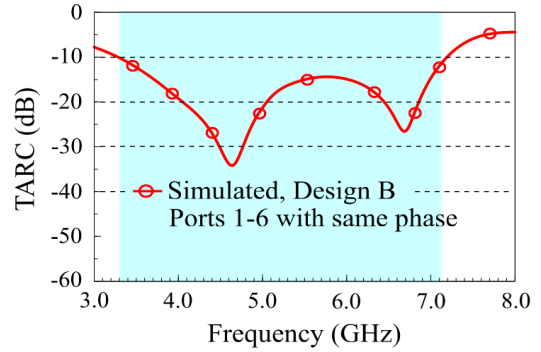


**FIGURE 10.** Simulated total active reflection coefficient (TARC) for Ports 1-6 with same phase in Design B.

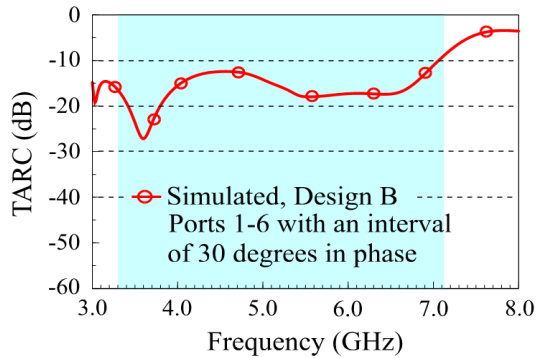


**FIGURE 11.** Simulated TARC for Ports 1-6 with an interval of 30 degrees in phase in Design B.

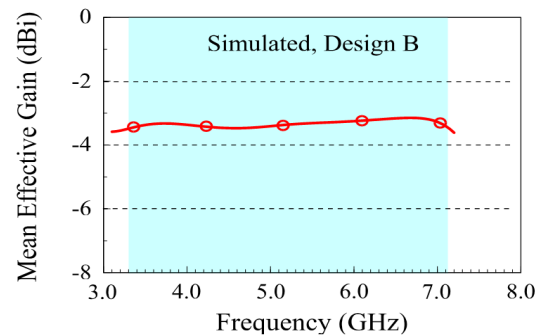


**FIGURE 12.** Simulated mean effective gain (MEG) of Port 1 in Design B.

### III. EXPERIMENTAL RESULTS AND DISCUSSION

The experimental results of Design B are presented to verify the simulation study. Fig. 14 shows the fabricated prototype of Design B in which the 0.2 mm thick copper plate is used to obtain an all-metal structure. Each port in Design B is respectively excited through a SMA connector attached on the back side of the ground plane. The measurement setup for the  $S$  parameters is shown in Fig. 15. Any two ports are measured with others terminated to  $50 \Omega$ .

The measured reflection coefficients of Ports 1-3 and 4-6 in the fabricated Design B are respectively shown in Fig. 16(a) and (b). It is seen that the measured data conform

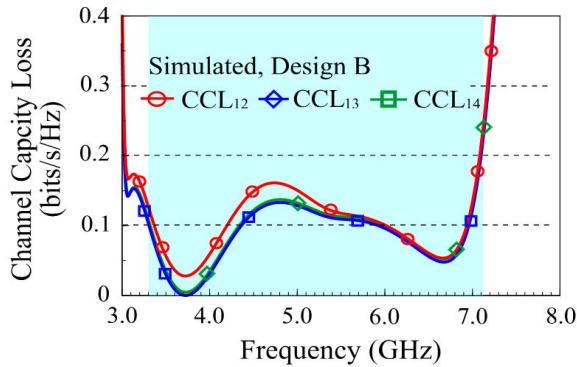


FIGURE 13. Simulated channel capacity loss (CCL) in Design B; the  $CCL_{ij}$  indicates the CCL between Ports  $i$  and  $j$ .

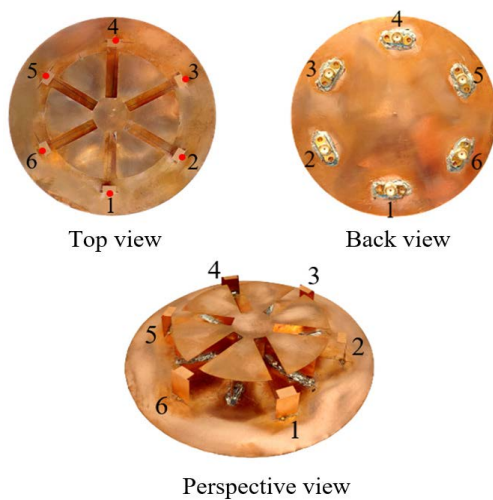


FIGURE 14. Fabricated prototype of Design B.

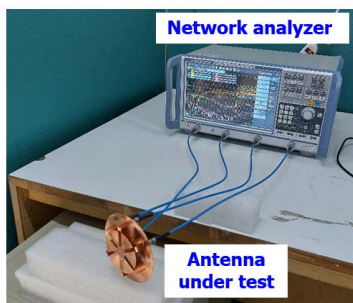


FIGURE 15. Measurement setup for the  $S$  parameters.

to the simulated results shown in the figure. It also shows that a wide operating band of larger than 3.3-7.125 GHz (colored frequency region in the figure) with impedance matching better than  $-10$  dB is obtained.

The representative measured transmission coefficients of Ports 1-6 in the fabricated Design B are shown in Fig. 17. The results for two nearby ports ( $S_{12}$ ,  $S_{23}$ ,  $S_{34}$ ,  $S_{45}$ ,  $S_{56}$ ) are shown in Fig. 17(a). Those for the two ports spaced by one  $60^\circ$ -sector ( $S_{13}$ ,  $S_{24}$ ,  $S_{35}$ ,  $S_{46}$ ) and spaced by two  $60^\circ$ -sectors ( $S_{14}$ ,  $S_{25}$ ,  $S_{36}$ ) are respectively shown in Fig. 17(b) and (c).

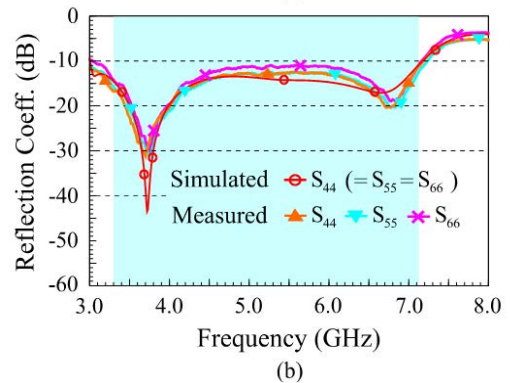
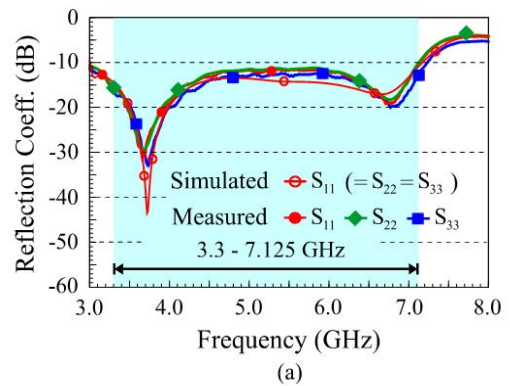


FIGURE 16. Measured and simulated reflection coefficients of the fabricated Design B. (a)  $S_{11}$ ,  $S_{22}$ ,  $S_{33}$ . (b)  $S_{44}$ ,  $S_{55}$ ,  $S_{66}$ .

The measured data also generally agree with the simulated results [the  $S_{i(i+1)}$  in Fig. 17(a), the  $S_{i(i+2)}$  in Fig. 17(b), the  $S_{i(i+3)}$  in Fig. 17(c)] and indicate that high port isolation ( $> 20$  dB) of Ports 1-6 is obtained over the wide band. Especially, those of the two ports spaced by one or two  $60^\circ$ -sectors show very high port isolation of larger than 30 dB over the wide band [see Fig. 17(b) and (c)].

The radiation performance is measured in a far-field anechoic chamber with a standard horn antenna used for calibration. The measurement setup for the fabricated prototype in the anechoic chamber is shown in Fig. 18. The measured antenna efficiencies of Ports 1-3 and Ports 4-6 in the fabricated Design B are respectively shown in Fig. 19(a) and (b). The corresponding measured antenna gain is also respectively shown in Fig. 20(a) and (b). The measured data generally conform to the simulated result of Port 1 (=Ports 2-6) included in the figure.

The measured antenna efficiency is larger than 85% over the antenna's operating band. The obtained high antenna efficiency is also attributed to the high port isolation, simple all-metal structure, and no external feed circuitry for the six-port SPA studied here. Additionally, the antenna gain is smoothly varied (the measured data varied from about 4.7 dBi to 6.2 dBi). This may also be attributed to the two resonances at about 3.6 and 6.6 GHz showing similar antenna performance as discussed in Section II.

Fig. 21 shows the measured and simulated normalized radiation patterns of Ports 1-3 at 3.6 GHz and 6.6 GHz



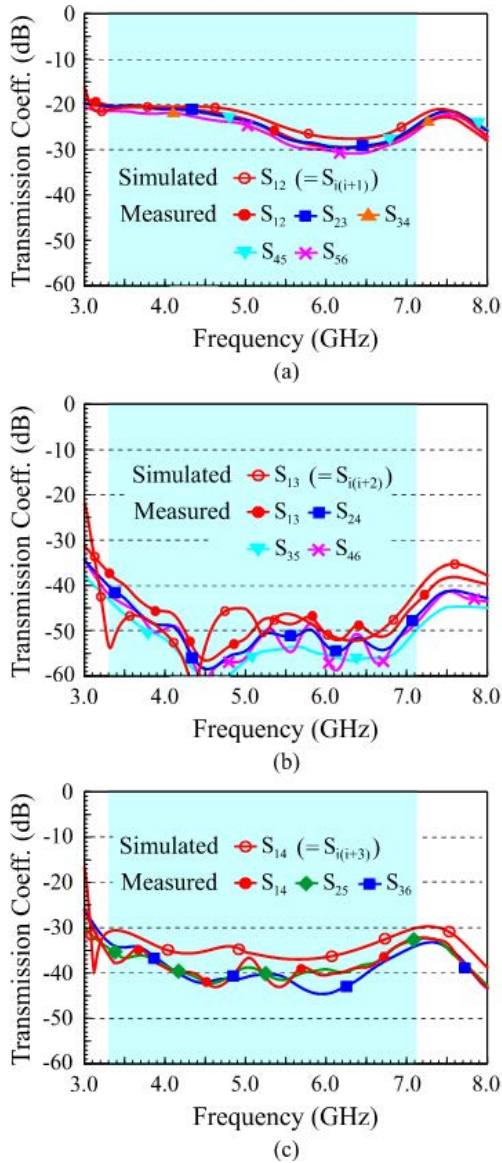


FIGURE 17. Measured and simulated transmission coefficients of the fabricated Design B. (a)  $S_{12}$ ,  $S_{23}$ ,  $S_{34}$ ,  $S_{45}$ ,  $S_{56}$ . (b)  $S_{13}$ ,  $S_{24}$ ,  $S_{35}$ ,  $S_{46}$ . (c)  $S_{14}$ ,  $S_{25}$ ,  $S_{36}$ .

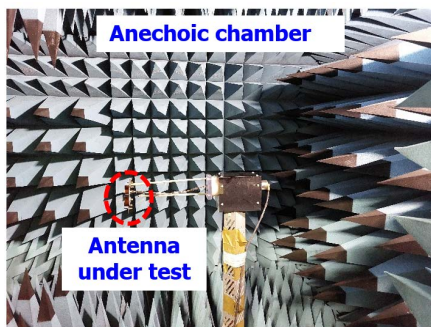


FIGURE 18. Radiation performance measurement setup in the anechoic chamber.

for Design B. The corresponding results of Ports 4-6 are plotted in Fig. 22. The radiation patterns of each port in the

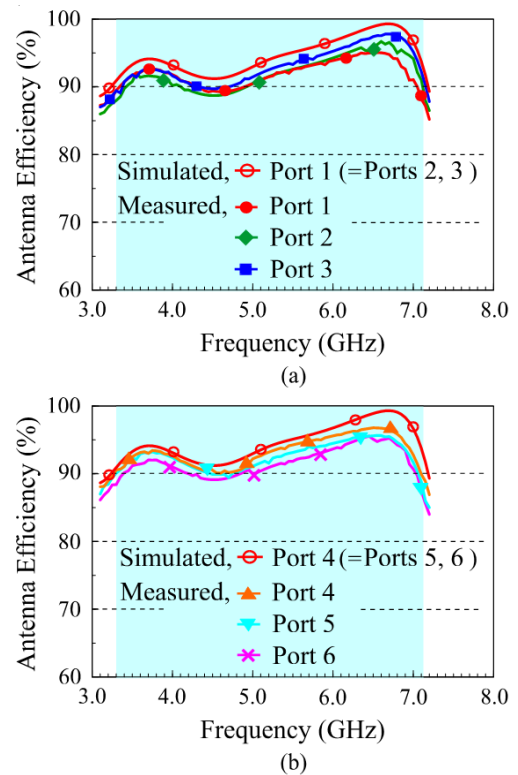


FIGURE 19. Measured antenna efficiency of the fabricated Design B. (a) Ports 1-3. (b) Ports 4-6. Simulated results are included for comparison.

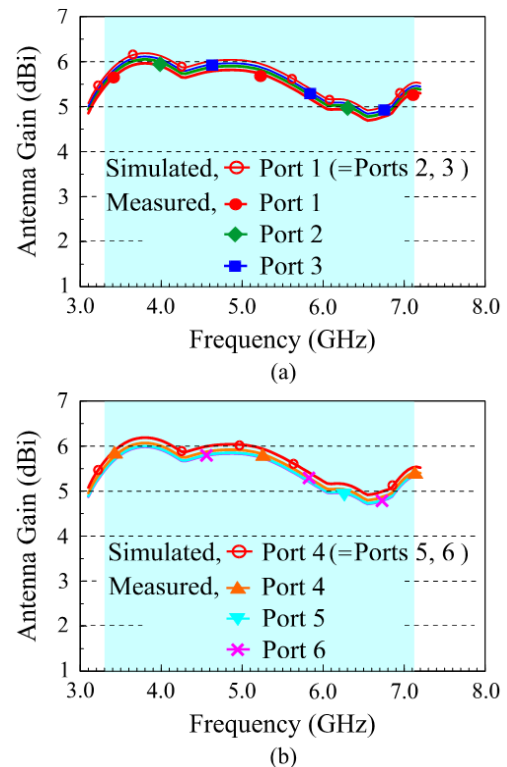
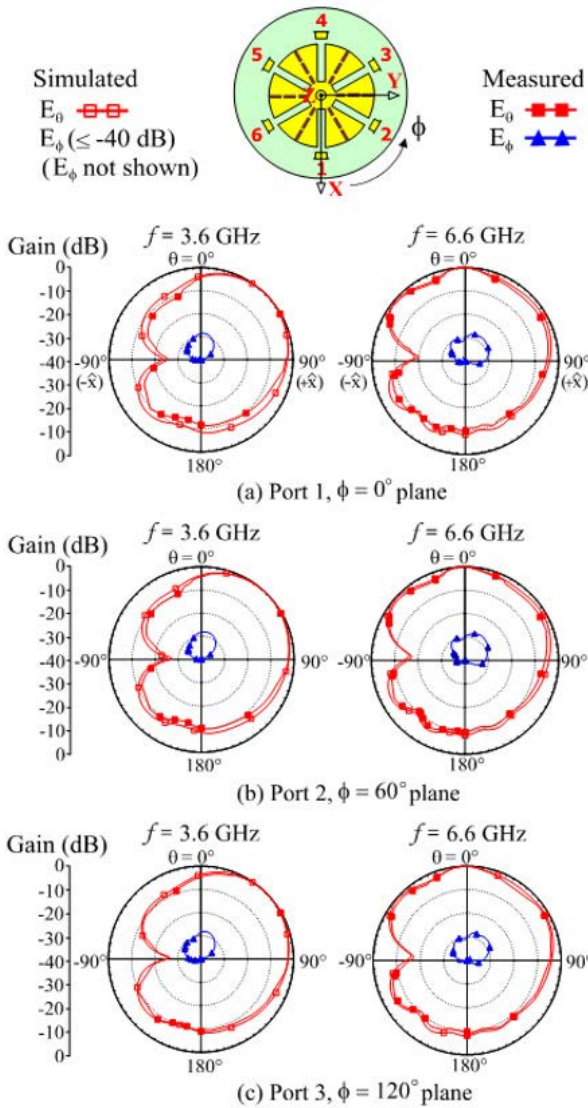


FIGURE 20. Measured antenna gain of the fabricated Design B. (a) Ports 1-3. (b) Ports 4-6. Simulated results are included for comparison.

plane along the centerline of its resonant sector are shown. For example, for Port 1 excitation, the radiation patterns



**FIGURE 21.** Measured and simulated normalized radiation patterns at 3.6 GHz and 6.6 GHz for Design B. (a) Port 1,  $\phi = 0^\circ$  plane. (b) Port 2,  $\phi = 60^\circ$  plane. (c) Port 3,  $\phi = 120^\circ$  plane.

at 3.6 GHz and 6.6 GHz in the  $\phi = 0^\circ$  plane (along the centerline of Sector 1) is shown in Fig. 21(a). For Port 2 and Port 3 excitation, the corresponding results in the  $\phi = 60^\circ$  plane (along the centerline of Sector 2) and in the  $\phi = 120^\circ$  plane (along the centerline of Sector 3) are presented in Fig. 21(b) and (c).

Similarly, the results for Port 4 in the  $\phi = 180^\circ$  plane (along the centerline of Sector 4), for Port 5 in the  $\phi = 240^\circ$  plane (along the centerline of Sector 5), and for Port 6 in the  $\phi = 300^\circ$  plane (along the centerline of Sector 6) are plotted in Fig. 21(a), (b), and (c). Good agreement of the measurement and simulation is obtained. Similar radiation patterns of Ports 1-6 are seen.

Also, for each port, its radiation patterns are seen to be tilted away from the  $z$  direction ( $\theta = 0^\circ$ ) toward the circular edge of the ground plane, especially in the direction of each

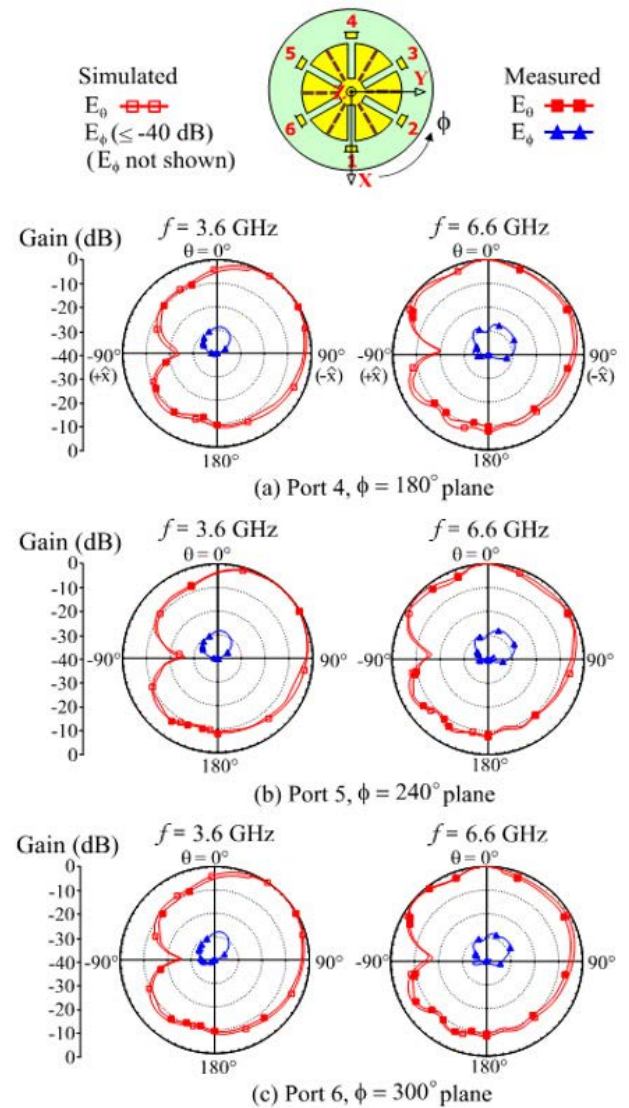


**FIGURE 22.** Measured and simulated normalized radiation patterns at 3.6 GHz and 6.6 GHz for Design B. (a) Port 4,  $\phi = 180^\circ$  plane. (b) Port 5,  $\phi = 240^\circ$  plane. (c) Port 6,  $\phi = 300^\circ$  plane.

port. This can be seen more clearly from the corresponding simulated three-dimensional (3-D) total-power radiation patterns at 3.6 and 6.6 GHz for Ports 1-3 and Ports 4-6 respectively shown in Figs. 23 and 24.

The  $E_\theta$  radiation is also seen to be dominant in the radiation pattern along the centerline of each sector, with the  $E_\phi$  radiation much weaker. Note that the simulated  $E_\phi$  component in the radiation plane along each sector's centerline is very weak (less than  $-40$  dB) and is not shown in the patterns in Figs. 21 and 22. This radiation characteristic can also be expected from the excited surface currents at 3.6 GHz and 6.6 GHz seen in Fig. 6.

Based on the measured three-dimensional radiation patterns [19], [22], the envelope correlation coefficients (ECCs) of any two radiating waves are also calculated. The ECC equation given in [19] is applied and representative ECC

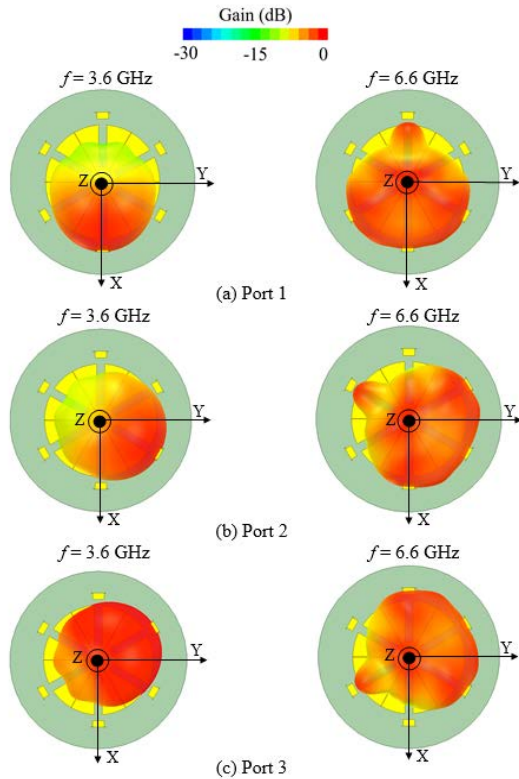


FIGURE 23. Simulated 3-D total-power radiation patterns at 3.6 and 6.6 GHz. (a) Port 1. (b) Port 2. (c) Port 3.

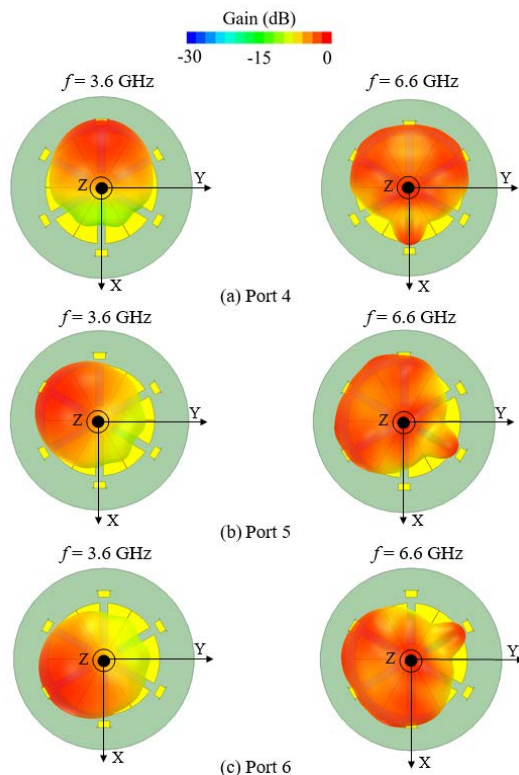


FIGURE 24. Simulated 3-D total-power radiation patterns at 3.6 and 6.6 GHz. (a) Port 4. (b) Port 5. (c) Port 6.

results are shown in Fig. 25. The  $ECC_{ij}$  indicates the correlation between the radiating waves of Ports  $i$  and  $j$ .

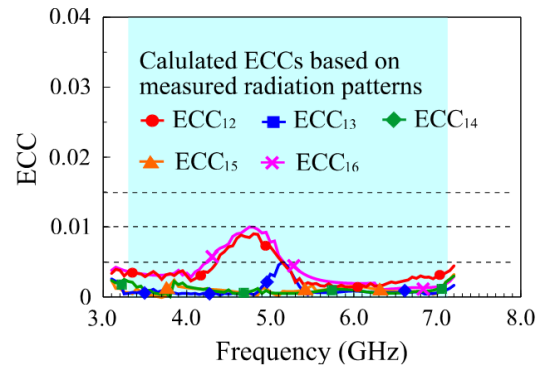


FIGURE 25. Calculated envelope correlation coefficients (ECCs) based on measured three-dimensional radiation patterns.

All the measured ECCs are less than 0.01 over the wide band. That is, very low correlation of the six radiating waves in the six-port SPA is obtained. Also note that the simulated ECCs based on using the simulated radiation patterns are even lower than 0.001 and are not shown in the figure for comparison. The very low ECCs are attractive for practical MIMO applications.

#### IV. CONCLUSION

A six-port SPA capable of radiating six uncorrelated waves over a very wide band (about 3.1-7.2 GHz in this study) has been proposed. The six-port antenna has the advantages of simple all-metal structure, high port isolation ( $>20$  dB), high antenna efficiency ( $>85\%$ ), and very low ECCs ( $<0.01$ ) over the very wide band of fractional bandwidth about 80%. Details of the antenna structure have been described. The design considerations and operating principle for generating the six uncorrelated waves over the very wide band have been addressed. The experimental results have also been shown to verify the simulation prediction. The six-port SPA is expected to be applicable for MIMO access-point applications.

#### REFERENCES

- [1] K.-L. Wong, C.-M. Chou, Y.-J. Yang, and K.-Y. Wang, "Multipolarized wideband circular patch antenna for fifth-generation multi-input–multi-output access-point application," *IEEE Antennas Wireless Propag. Lett.*, vol. 18, no. 10, pp. 2184–2188, Oct. 2019.
- [2] C.-Y. Chiu, S. Shen, B. K. Lau, and R. D. Murch, "The design of a trimodal broadside antenna element for compact massive MIMO arrays: Utilizing the theory of characteristic modes," *IEEE Antennas Propag. Mag.*, vol. 62, no. 6, pp. 46–61, Dec. 2020.
- [3] C.-Y. Chiu, B. K. Lau, and R. Murch, "Bandwidth enhancement technique for broadside tri-modal patch antenna," *IEEE Open J. Antennas Propag.*, vol. 1, pp. 524–533, 2020.
- [4] K. L. Wong and G. L. Yan, "Wideband three-port equilateral triangular patch antenna generating three uncorrelated waves for 5G MIMO access points," *IEEE Access*, vol. 10, pp. 893–899, 2022.
- [5] K.-L. Wong, X.-Q. Ye, and W.-Y. Li, "Wideband four-port single-patch antenna based on the quasi-TM<sub>1/2,1/2</sub> mode for 5G MIMO access-point application," *IEEE Access*, vol. 10, pp. 9232–9240, 2022.
- [6] K. L. Wong, M. F. Jian, and W. Y. Li, "Low-profile wideband four-cornered square patch antenna for 5G MIMO mobile antenna application," *IEEE Antennas Wireless Propag. Lett.*, vol. 20, no. 12, pp. 2054–2058, Dec. 2021.

- [7] K.-L. Wong, J.-Z. Chen, and W.-Y. Li, "Four-port wideband annular-ring patch antenna generating four decoupled waves for 5G multi-input-multi-output access points," *IEEE Trans. Antennas Propag.*, vol. 69, no. 5, pp. 2946–2951, May 2021.
- [8] N. L. Johannsen, N. Peitzmeier, P. A. Hoehner, and D. Manteuffel, "On the feasibility of multi-mode antennas in UWB and IoT applications below 10 GHz," *IEEE Commun. Mag.*, vol. 58, no. 3, pp. 69–75, Mar. 2020.
- [9] W. Su, Q. Zhang, S. Alkaraki, Y. Zhang, X.-Y. Zhang, and Y. Gao, "Radiation energy and mutual coupling evaluation for multimode MIMO antenna based on the theory of characteristic mode," *IEEE Trans. Antennas Propag.*, vol. 67, no. 1, pp. 74–84, Jan. 2019.
- [10] N. Peitzmeier, T. Hahn, and D. Manteuffel, "Systematic design of multimode antennas for MIMO applications by leveraging symmetry," *IEEE Trans. Antennas Propag.*, vol. 70, no. 1, pp. 145–155, Jan. 2022.
- [11] J.-S. Row, S.-H. Yeh, and K.-L. Wong, "A wide-band monopolar plate-patch antenna," *IEEE Trans. Antennas Propag.*, vol. 50, no. 9, pp. 1328–1330, Sep. 2002.
- [12] (Jan. 2020). *White Paper of GSA (the Global Mobile Suppliers Association). 3300–4200 MHz: A Key Frequency Band for 5G*. [Online]. Available: <https://gsacom.com/paper/3300-4200-mhz-a-key-frequency-band-for-5g/>
- [13] (Mar. 23, 2020). *CTIA (Cellular Telecommunications Industry Association) Report. 5G Mid-Band Spectrum Global Update*. [Online]. Available: <https://www.ctia.org/news/report-5g-mid-band-spectrum-global-update>
- [14] (Nov. 6, 2019). *WRC-19 (World Radiocommunication Conference 2019) Report. Key Outcomes of the WRC-19*. [Online]. Available: <https://www.itu.int/en/itu-news/Documents/2019/2019-06/2019-ITUNews06-en.pdf>
- [15] C.-T. Lee and K.-L. Wong, "Uniplanar printed coupled-fed PIFA with a band-notching slit for WLAN/WiMAX operation in the laptop computer," *IEEE Trans. Antennas Propag.*, vol. 57, no. 4, pp. 1252–1258, Apr. 2009.
- [16] K.-H. Kim and K.-J. Ahn, "The high isolation dual-band inverted F antenna diversity system with the small N-section resonators on the ground plane," *Microw. Opt. Technol. Lett.*, vol. 49, no. 3, pp. 731–734, 2007.
- [17] (Mar. 1, 2022). *3D High Frequency Electromagnetic Simulation Software, ANSYS HFSS*. [Online]. Available: <https://www.ansys.com/products/electronics/ansys-hfss>
- [18] M. Manteghi and Y. Rahmat-Samii, "Multiport characteristics of a wide-band cavity backed annular patch antenna for multipolarization operations," *IEEE Trans. Antennas Propag.*, vol. 53, no. 1, pp. 466–474, Jan. 2005.
- [19] M. S. Sharawi, "Printed multi-band MIMO antenna systems and their performance metrics," *IEEE Antennas Propag. Mag.*, vol. 55, no. 5, pp. 218–232, Oct. 2013.
- [20] S. H. Chae, S.-k. Oh, and S.-O. Park, "Analysis of mutual coupling, correlations, and TARC in WiBro MIMO array antenna," *IEEE Antennas Wireless Propag. Lett.*, vol. 6, pp. 122–125, 2007.
- [21] M. Khalid, S. I. Naqvi, N. Hussain, M. Rahman, Fawad, S. S. Mirjavadi, M. J. Khan, and Y. Amin, "4-port MIMO antenna with defected ground structure for 5G millimeter wave applications," *Electronics*, vol. 9, no. 1, p. 71, Jan. 2020.
- [22] S. Blanch, J. Romeu, and I. Coebella, "Exact representative of antenna system diversity performance from input parameter description," *Electron. Lett.*, vol. 39, pp. 705–707, May 2003.

Professor, in 1991. From 1998 to 1999, he was a Visiting Scholar with the ElectroScience Laboratory, The Ohio State University, Columbus, OH, USA. He was elected to be the Sun Yat-sen Chair Professor of NSYSU, in 2005; a Distinguished Chair Professor of NSYSU, in 2017; and the National Chair Professor of the Ministry of Education of Taiwan, in 2016. He has also worked as the Chairperson of the Electrical Engineering Department, from 1994 to 1997; the Vice President for research affairs, from 2005 to 2007; and the Senior Vice President of NSYSU, from 2007 to 2012. He is currently the National Chair Professor of the Ministry of Education, a Distinguished Researcher of the Ministry of Science and Technology, and a Distinguished Chair Professor with NSYSU. He has authored more than 580 refereed journal articles and 300 conference papers. He has personally supervised 57 graduated Ph.D.s. He holds over 300 patents, including 102 U.S. patents. He is the author of *Design of Nonplanar Microstrip Antennas and Transmission Lines* (Wiley, 1999), *Compact and Broadband Microstrip Antennas* (Wiley, 2002), and *Planar Antennas for Wireless Communications* (Wiley, 2003). His published articles have been cited over 33,300 times with an H-index of 87 in Google Scholar. In 2022, he was selected by Research.com to be ranked #99 in Full World Ranking and #1 in Full Taiwan Ranking in the 2022 Edition of Ranking of Top 1000 Scientists in the field of electronics and electrical engineering.

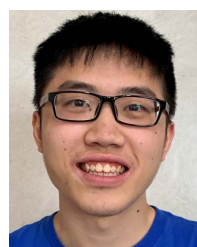
Dr. Wong has served or serves as an IEEE AP-S AdCom Member, an IEEE AP-S Transactions Track Editor/Associate Editor, an AP-S Transactions Paper Awards Committee Member, and an AP-S Field Awards Committee Member. He was also a PE7 Panel Member of 2015, 2017, and 2019 European Research Council Advanced Grant Panel and a Chief Consultant of the Institute of Antenna Engineers of Taiwan. In 2008, the research achievements on handheld device antennas of NSYSU Antenna Laboratory led by him was selected to be top 50 scientific achievements of Taiwan Ministry of Science and Technology in past 50 years (1959–2009). He was a recipient of the 2010 Outstanding Research Award of Pan Wen Yuan Foundation and selected as top 100 Honor of Taiwan by Global Views Monthly, in August 2010, for his contribution in mobile antenna researches. He was also a recipient of the Academic Award (2012) from Taiwan Ministry of Education and the Outstanding Distinguished Researcher Award (2013) from Taiwan Ministry of Science and Technology. He was awarded the Best Associate Editor two times (2015 and 2016) for the IEEE TRANSACTIONS ON ANTENNAS AND PROPAGATION. He has received the Outstanding Research Award three times (1995, 2000, and 2002) from Taiwan National Science Council. He has also received the Outstanding Electrical Engineering Professor Award (2003) from the Institute of Electrical Engineers of Taiwan and the Outstanding Engineering Professor Award (2004) from the Institute of Engineers of Taiwan. He and his graduate students have been awarded the Best Paper Award (APMC Prize) in 2008 APMC and the Best Student Paper Award/Young Scientist Award in 2007 ISAP, 2008 APMC, 2009 ISAP, 2010 ISAP, 2012 ISAP, and 2016 ISAP. His graduate students also won the First Prize of 2007 and 2009 Taiwan National Mobile Handset Antenna Design Competition. He has served as the General Chair for 2012 APMC, 2014 ISAP, and 2016 APCAP at Kaohsiung, Taiwan. He has also served as the Chair for the Judge Panel for 2014–2021 National Communication Antenna Design Competition organized by Taiwan Ministry of Economics. He was elected as a Thomson Reuters Highly Cited Researcher, in 2014 and 2015, and also elected as an Elsevier Most Cited Researcher, in 2015. He is a Thomson Reuters Highly Cited Researcher and an Elsevier Most Cited Researcher.



Sun Yat-sen University (NSYSU), Kaohsiung, Taiwan, where he became a

**KIN-LU WONG** (Fellow, IEEE) received the B.S. degree in electrical engineering from the National Taiwan University, Taipei, Taiwan, in 1981, and the M.S. and Ph.D. degrees in electrical engineering from Texas Tech University, Lubbock, TX, USA, in 1984 and 1986, respectively.

From 1986 to 1987, he was a Visiting Scientist with the Max-Planck-Institute for Plasma Physics, Munich, Germany. Since 1987, he has been with the Electrical Engineering Department, National



**ZONG-WEN TSO** (Student Member, IEEE) received the B.S. degree in electrical engineering from the National Chi Nan University, Nantou County, Taiwan, in 2021. He is currently pursuing the M.S. degree with the National Sun Yat-sen University, Kaohsiung, Taiwan. His main research interests include multi-port MIMO wide-band patch antennas for 5G/5G+ access-point and mobile-device applications.



**WEI-YU LI** (Member, IEEE) was born in Taipei, Taiwan, in 1981. He received the B.S. degree in electrical engineering from Feng Chia University, Taichung, Taiwan, in 2004, and the M.S. and Ph.D. degrees in electrical engineering from the National Sun Yat-sen University (NSYSU), Kaohsiung, Taiwan, in 2006 and 2009, respectively.

After graduated from NSYSU, in 2009, he has been with the Information and Communication Research Laboratories (ICL), Industrial Technology Research Institute (ITRI), Hsinchu, Taiwan, participating and leading advanced research for development of emerging wireless antenna technologies. From April 2012 to October 2012, he was an Exchange Guest Researcher with the National Institute of Information and Communications Technology (NICT), Tokyo, Japan. He is currently a Deputy Technology Manager of ITRI. He has authored and coauthored 30 refereed journal articles and 40 conference papers. He holds over 70 patents, including U.S., Taiwan, China, and EU patents. His published articles have been cited over 1,300 times with an H-index of 21 in Google Scholar.

Dr. Li has been selected as an International Steering Committee Member of 2019–2021 ISAP and the Chair of IEEE AP-S Tainan Chapter in 2021–2022. He also served as an AdCom Member for the Institute of Antenna Engineers of Taiwan, in 2014 and 2015, and in 2018–2022. He also served as a one member for the Judge Panel for 2014 to 2022 National Terminal Antenna Design Competition organized by the Taiwan Ministry of Economics. He has received the Young Scientist Award in 2007 ISAP and the Best Paper Award (APMC Prize) in 2008 APMC. He has been a principal investigator or a co-principal investigator of many research projects at ITRI and has received numerous recognitions, including the First Prize of the Outstanding Research Award of ITRI, in 2010; the Solar Industrial Award (SIA) of Europe, in 2011; the Outstanding Innovation Award of ITRI, in 2013; the Second Prize of the Outstanding Research Award of ITRI, in 2014; the 2015 Research and Development 100 Award Finalist of the USA; the Outstanding Innovation Award of ITRI, in 2017; the First Prize of the Outstanding Industrialization Award of ITRI, in 2017; the Second Prize of the Outstanding Industrialization Award of ITRI, in 2020; and the Third Prize of the Outstanding Industrialization Award of ITRI, in 2021. He has also received the Outstanding Lecturer Award of ITRI, in 2013; and the International Paper Award of ICL of ITRI, in 2020.

• • •